



New Schiff base copper(II) and nickel(II) complexes for biomedical applications with reference to SARS-CoV-2 and HIV virus

Aprajita & Mukesh Choudhary*

Department of Chemistry, National Institute of Technology Patna, Patna -800 005, Bihar, India

*E-mail: mukesh@nitp.ac.in

Received 23 March 2022; accepted (revised) 26 May 2022

A series of nickel(II) and copper(II) complexes viz. $[\text{Ni}(\text{L}^1)_2](\mathbf{1})$, $[\text{Cu}(\text{L}^1)_2](\mathbf{2})$, $[\text{Ni}(\text{L}^2)_2](\mathbf{3})$ and $[\text{Cu}(\text{L}^2)_2](\mathbf{4})$ (where $\text{L}^1\text{H}=(E)\text{-N-phenyl-2-(thiophen-2-ylmethylene)hydrazine-1-carboxamide}$, $\text{L}^2\text{H}=(E)\text{-2-((3-methylthiophen-2-yl)methylene)-N-phenylhydrazine-1-carbothioamide}$), have been synthesized and designed as potential inhibitors against SARS-CoV-2 and HIV-1 virus. The quantum computational calculations are used for structure-property relationship. A detailed structural and non-covalent supramolecular interaction in the ligand (L^1H) is investigated by single crystal structure analysis and computational approaches. Hirshfeld surface analysis is done in the crystal structure of the ligand (L^1H), while 3D topology of the crystal packing is visualized through an energy framework. To find potential inhibitors of the SARS-CoV-2 and HIV-1 virus, molecular docking of the ligands and their corresponding metal complexes with SARS-CoV-2 and HIV-1 virus is performed. The X-ray crystallographic structure of the main protease of the SARS-CoV-2 (PDB ID: 7VNB) and HIV-1 virus (PDB ID: 1REV) is retrieved from the protein data bank and used as receptor proteins. The molecular docking results has shown that Schiff bases and their complexes with SARS-CoV-2 and HIV-1 virus exhibited good binding affinity at binding site of receptor protein. It is also observed that the binding affinities of the Schiff bases and metal complexes towards SARS-CoV-2 are comparatively higher than the HIV virus. This study may offer the new antiviral drug candidates against SARS-CoV-2 and HIV-1 virus.

Keywords: Schiff base, Metal complexes, SARS-CoV-2, HIV virus, Quantum computation study

Semicarbazone and thiosemicarbazones are important Schiff base ligands having multidentate coordinating sites, essential to synthesize new metal-complexes with multiple pharmacological applications¹⁻⁴. They are extensively used as ligands in studying the anti-viral and antimalarial activity of metal complexes due to their rich biological, medicinal and pharmacological properties^{5,6}. They can coordinate to different metal centre as neutral molecules or as anionic ligands. Semicarbazone can bind through their oxygen while thiosemicarbazones coordinate through their sulphur and azomethine imine nitrogen atom with transition metal ion, making them good chelating agents^{7,8}. Previously, it has been studied that in citronellal thiosemicarbazone derivative bis complexes of nickel metal, where the Schiff base ligand was coordinated to the metal centre through its bidentate N and S atom, was efficiently active towards several cancer cell lines⁹. However, not much has been studied on ligands and complexes derived from thiophene-2-carboxaldehyde. Nickel and copper are found to be important bio element in the field of bioinorganic chemistry since they are present in several enzymes¹⁰. For instance, nickel is present as

the fragment of active sites of hydrogenase and carbon monoxide dehydrogenases¹¹. Moreover, nickel and copper complexes have excellent antimicrobial, antiproliferative, anti-viral and anticancer properties^{12,13}.

The SARS-CoV-2 main protease plays a significant role in viral replication. Due to its low similarity with human genes, it is a crucial target for designing and discovering novel SARS-CoV-2 drugs. Investigation of binding affinity and structure-property relationship of protein-drug complexes plays an essential role in understanding the molecular mechanism for drug discovery^{14,15}. It is urgent to identify effective and active antiviral compounds that can block the infection at the individual stage and stop its spread worldwide. One target that has received much attention is the SARS-CoV-2 main protease (M^{pro})¹⁶⁻¹⁸, a homodimer whose crystal structure has been determined¹⁹. SARS-CoV-2 causes infected cells to express a main protease (M^{pro} or 3CL protease) that is responsible for site-specifically cleaving the polyprotein, which is translated from viral m-RNA within human cells²⁰. The proteolytic activity of M^{pro} is essential to the virus to generate the individual

proteins that are necessary for replication and infection. The essential role of M^{pro} , as well as the success of HIV protease inhibitors in the treatment of HIV/AIDS, makes M^{pro} an attractive therapeutic target to treat SARS-CoV-2²¹. It is on January 7, 2020, that Chinese scientists attempted to isolate SARS-CoV-2 and finally sequenced the genome SARS-CoV-2. They also pointed out a potential drug target protein for the inhibition of SARS-CoV-2 replication²².

Herein, a series of Ni(II) and Co(II) complexes viz. $[Ni(L^1)_2](1)$, $[Cu(L^1)_2](2)$, $[Ni(L^2)_2](3)$ and $[Cu(L^2)_2](4)$ of (*E*)-*N*-phenyl-2-(thiophen-2-ylmethylene)hydrazine-1-carboxamide (**L¹H**) and (*E*)-2-((3-methylthiophen-2-yl)methylene)-*N*-phenylhydrazine-1-carbothioamide (**L²H**) as potential inhibitors against SARS-CoV-2 and HIV-1 virus, were designed, synthesized, and characterized. This study may offer the new antiviral drug candidates against SARS-CoV-2 and HIV-1 virus.

Experimental Details

Chemicals

All chemicals used in this analysis were of analytical grade and used as procured. 4-Phenyl semicarbazide hydrochloride, thiophene-2-carbaldehyde, 4-phenylthiosemicarbazide, 3-methyl-2-thiophene carbaldehyde, copper(II) acetate monohydrate, nickel(II) acetate tetrahydrate salt were obtained from Sigma-Aldrich and used without further purification.

Characterization techniques

Various physical and spectral methods (NMR, FT-IR and UV-visible spectroscopy) were investigated for the characterization of the ligand and complexes. Elemental analytical data and quantum mechanical calculations are also applied for these purposes. The electronic spectra of the compounds were taken on a Thermo scientific UV-Vis recording spectrophotometer Evolution-3000 in quartz cells. NMR spectra were recorded on a Bruker Advance HD 500 MHz FT-NMR Spectrometer. IR spectra were recorded in KBr medium on a Bruker-Alpha-Platinum-ATR spectrophotometer (500-4000 cm^{-1}). The C, H, and N determinations were made on an Elementar Vario EL III Carlo Erba 1108 analyzer.

Crystal structure determination

The single crystal X-ray diffraction data of the ligand **L¹H** collected at 296(2) K using Bruker SMART APEXII CCD diffractometer, equipped with

graphite-crystal incident beam monochromator, and a fine focus sealed tube with Mo-K α ($\lambda = 1.54178 \text{ \AA}$) and the X-ray source at the SAIF, IIT Madras, India. The Bruker SMART and Bruker SAINT softwares were used for data acquisition and data reduction, respectively. The structures were solved by direct methods and refined by full-matrix least-square calculations with the SHELXL-2018/3 software package²³. All non-hydrogen atoms were refined anisotropically, and all hydrogen atoms on carbon were placed in calculated positions, guided by difference maps and refined isotropically. The molecular and crystal structures were plotted using ORTEP, PLATON, Mercury and Diamond 3.2 k²⁴ programs.

Powdered X-ray diffraction study

Powder XRD patterns of the ligands and complexes are recorded on Bruker D8 X-ray diffractometer with Cu as anode material^{25,26}. The pattern was recorded in the 2θ range of 0° to 80° with a potential difference of 40 kV and current 30 mA using Cu K α radiation at $\lambda = 0.15406 \text{ nm}$ at a scan rate of $0.02^\circ \text{ min}^{-1}$. Crystal size (*D*) was estimated by Scherrer's formula, $D = k\lambda/\beta\cos\theta$, *k* is a constant ($k = 0.94$), λ is the wavelength used ($\lambda = 0.154 \text{ nm}$), β width at half maxima (FWHM) of the whole peaks by XRD patterns while θ is Bragg angle.

Hirshfeld surface analysis

The Hirshfeld surface (HS) is a useful graphical visualization tool used to analyze the nature of the intermolecular interactions in the crystal packing, quantified using the Crystal Explorer 17.5 software²⁷. The HS provides qualitative information about all intermolecular interactions at a time, whereas fingerprint plots produce the most efficient interactive graphics to obtain intermolecular interactions quantitatively inside the crystal packing²⁸. The molecular HS and their associated two-dimensional fingerprint plots (FPs) were generated for Schiff base ligand **L¹H** based on their crystallographic information file (cif), using *CrystalExplorer 17.5* software. The 3D graphical plots of the HSs are mapped over the d_{norm} (normalized contact distance) surface enables us to visualize the various intermolecular interactions in the crystal lattice and allows us to gain insight into the crystal packing behaviour. The HS is reduced to 2D fingerprint plots by obtaining standard resolution of molecular HS on calculating the d_i and d_e for each surface point. The d_i

and d_e are the distance to the HS from the nearest internal nucleus (inside the HS) and external nucleus (outside the HS), respectively. Further, the data are binned into a discrete interval of d_i and d_e , to generate a 2D histogram with a scale of 0.2 Å. The 2D FPs give a summary of the frequency of each combination d_i and d_e across the surface of a molecule and indicates the interactions present as well as the relative area of the surface corresponding to those interactions²⁹. The energy framework analysis is carried out in order to explore the intermolecular interaction energies between the molecular pairs within the cluster of radii 3.8 Å. These calculations were performed using *Crystal Explorer 17.5* combined with CE-B3LYP/6-31G(d,p) functional/basis set. The radius of the cylinder connected to the centroids of the pairs of molecules represents the magnitude of interaction energies and relative strength of the molecular packing in a different direction. Using energy framework analysis, supramolecular architecture of the crystal structure can be visualized^{30,31}.

Theoretical study

Theoretical calculations by density functional theory (DFT) were performed with regard to molecular structure optimization and HOMO-LUMO energies, etc. of all synthesized compounds. The geometry optimization of the ligands and complexes was performed at the ω B97X-D/6-311+G** level of theory in vacuum using the Gaussian16 software package³² and cross-validated using the Spartan 16/18 parallel suite of programs³³ at the resources of the computational facility at Department of Chemistry, NIT Patna, India. The dispersion-corrected DFT functional ω B97X-D³⁴ was chosen to accurately estimate the van der Waals interactions, which are expected to contribute greatly to the stability of the complexes. Global reactivity descriptors, such as ionization potential (IP), electron affinity (EA), electro negativity (χ), chemical potential (μ), global hardness (η), global softness (σ) and global electrophilicity (ω), were calculated using the formulas based on Koopmans theorem³⁵.

Molecular docking study

The molecular docking studies were performed for all the synthesized compounds to analyze their binding affinity for selected virus proteins. The crystal structures of SARS-CoV-2 main protease³⁶ (PDB ID: 7VNB; Space group: *H3*; unit cell: a = 146.21Å, b =

146.21Å, c = 93.08Å, $\alpha = 90^\circ$, $\beta = 90^\circ$, $\gamma = 120^\circ$) and crystal structure of HIV-1 virus³⁷ (PDB ID: 1REV; Space group: *HP2₁2₁2₁*; unit cell: a = 138.8 Å, b = 115.8 Å, c = 66.2 Å, $\alpha = 90^\circ$, $\beta = 90^\circ$, $\gamma = 90^\circ$) was obtained from the Protein Data Bank and used as receptor proteins. Initially, the protein coordinates were refined by deleting all the water and heteroatoms to make the targeted protein receptor-free. Further, the polar hydrogens and Kollman charges were added to the protein using the *Autodock tool* (ADT) 1.5.6 associated with *Autodock 4.2* software³⁸. The prepared protein and ligand coordinates are saved in a pdbqt file format using ADT software. The grid box of the desired volume is selected in such a way that the ligand can rotate freely inside the active site pocket protein. The configuration files are generated using the coordinates and dimension of the grid box. *Vina Lamarckian* genetic algorithm³⁹ generates the output files having predicted free energy for binding sites. The result comprising of different poses with corresponding energies were analyzed and high-quality figures are rendered by open-source Discovery Studio visualizer⁴⁰.

Synthesis procedure

(E)-N-phenyl-2-(thiophen-2-ylmethylene)hydrazine-1-carboxamide (L¹H)

To synthesize L¹H, 4-phenyl semicarbazide hydrochloride (2.0 mmol, 0.375 g) was taken in ethanol (10 mL) with dropwise addition of ethanolic solution of thiophene-2-carbaldehyde (2.0 mmol, 0.27 mL). The stirred mixture was refluxed for 2-3 h. White colour shiny crude product was obtained. XRD quality needled shaped single crystals were obtained by the slow evaporation of its methanol solution in air. Anal. Calcd for L¹H; C₁₂H₁₁N₃OS (245.30 g/mol) C, 58.76%; H, 4.52%; N, 17.13%. Found: C, 58.76%; H, 4.39%; N, 17.11%. FAB-mass (m/z): Obs. (Calcd.) 245.06 (245.3 g/mol.); ¹H-NMR (500 MHz, DMSO-d₆): δ 8.62 (s, 1H, -N=CH), δ 7.58-7.63 (m, 3H, Ar-H), δ 7.43 (s, 1H, Ar-H), δ 8.15 ppm (H, -N-H), δ 10.68 ppm (H, -N-H) (Fig. S1). ¹³C-NMR (500 MHz, DMSO-d₆): δ 153.18, 139.40, 139.379, 136.72, 129.91, 128.49, 128.23, 122.97, 120.031 and 39.59 ppm (Fig. S2). IR data (KBr/cm⁻¹): 1593 (>C=N); 3171(v N-H); 3364 (v O-H). UV-visible (DMSO) λ (nm): 340(π - π^*) and 306 (n- π^*).

(E)-2-((3-methylthiophen-2-yl)methylene)-N-phenylhydrazine-1-carbothioamide (L²H)

To synthesize L²H, 4-phenylthiosemicarbazide (2.0 mmol, 0.334 g) was taken in ethanol (10 mL)

with dropwise addition of ethanolic solution of 3-methyl-2-thiophene carbaldehyde (2 mmol, 0.29 mL). The stirred mixture was refluxed for 2-3 h. Light brown colour shiny crude product was obtained. Anal. Calcd for **L²H**; C₁₃ H₁₃N₃S₂ (275.39 g/mol) C, 56.07%; H, 4.76%; N, 15.26%. Found: C, 56.07%; H, 4.73%; N, 15.22%. FAB-mass (m/z): Obs. (Calcd.) 275.06 (275.39 g/mol.); ¹H-NMR (500 MHz, DMSO-d₆): δ 8.25 (s, 1H, -N=CH), δ 7.35 (s, 1H, Ar-H), δ 7.57 (s, 1H, Ar-H), δ 9.72 ppm (H, -N-H), δ 11.77 ppm (H, -N-H) (Fig. S3). ¹³C-NMR (500 MHz, DMSO-d₆): δ 175.70, 141.07, 139.43, 138.22, 132.30, 131.42, 128.77, 128.59, 125.62, 125.57, 14.17 and 40.01 ppm (Fig. S4). IR data (KBr/cm⁻¹): 1591 (>C=N); 2326 (ν S-H); 3292(ν N-H). UV-visible (DMSO) λ (nm): 368 (π-π*) and 325 (n-π*).

Synthesis of complex [Ni(L¹)₂] (1)

To a solution of **L¹H** (1 mmol, 0.245 g) in methanol (10 mL), triethylamine (1.0 mmol, 0.68 mL) is added dropwise. The mixture was stirred for half an hour. This mixture was then added dropwise to the methanolic solution of nickel (II) acetate tetrahydrate salt (0.5 mmol, 0.124 g). After the completion of the reaction, the reaction mixture was filtered and was left for slow evaporation at RT. Light brown colour weak crystals was obtained. Anal. Calcd for (1); C₂₄H₂₀N₆NiO₂S₂ (547.28 g/mol) C, 52.67%; H, 3.68%; N, 15.36%. Found: C, 52.66%; H, 3.66%; N, 15.35%. FAB-mass (m/z): Obs. (Calcd.) 547.28 (547.26 g/mol.); UV-visible (DMSO) λ (nm): 350 (π-π*) and 309 (n-π*).

Synthesis of complex [Cu(L¹)₂] (2)

The complex (2) was synthesized in a similar fashion as complex (1) by adding copper (II)acetate monohydrate salt (0.5 mmol, 0.100 g) instead of nickel(II) acetate tetrahydrate salt. The resultant solution was stirred for 4-5 h. After the completion of the reaction, the reaction mixture was filtered and was left for slow evaporation at RT. The obtained light green colour residue was filtered off and dried under reduced pressure. Anal. Calcd for (2); C₂₄H₂₀CuN₆O₂S₂ (551.04 g/mol) C, 52.21%; H, 3.65%; N, 15.22%. Found: C, 52.21%; H, 3.64%; N, 15.19%. FAB-mass (m/z): Obs. (Calcd.) 551.04 (551.02 g/mol.); UV-visible (DMSO) λ (nm): 348 (π-π*) and 313 (n-π*).

Synthesis of complex [Ni(L²)₂] (3)

To a solution of **L²H** (1 mmol, 0.275 g) in acetonitrile (10 mL), triethylamine (1 mmol, 0.680 mL) is added

dropwise. The mixture was stirred for half an hour. This mixture was then added dropwise to the methanolic solution of nickel(II) acetate tetrahydrate salt (0.5 mmol, 0.124 g). The resultant solution was stirred for 4-5 h. After the completion of the reaction, the reaction mixture was filtered and was left for slow evaporation at RT. Brown colour residue was obtained. Anal. Calcd for (3); C₂₆H₂₄N₆NiS₄ (607.45 g/mol) C, 51.41%; H, 3.98%; N, 13.84%. Found: C, 51.40%; H, 3.97%; N, 13.86%. FAB-mass (m/z): Obs. (Calcd.) 607.45 (607.43 g/mol.); UV-visible (DMSO) λ (nm): 352 (π-π*) and 283 (n-π*). IR data (KBr/cm⁻¹): 1589 (ν>C=N); 610 (νNi-S), 543 (ν Ni-N).

Synthesis of complex [Cu(L²)₂] (4)

The complex (4) was synthesized in a similar fashion as complex (3) by adding copper(II) acetate monohydrate salt (0.5 mmol, 0.100 g) instead of nickel(II) acetate tetrahydrate salt. The resultant solution was stirred for 4-5 h. The obtained dark green colour precipitate was filtered off and dried under reduced pressure. Anal. Calcd for (4); C₂₆H₂₄CuN₆S₄ (612.31 g/mol) C, 51.00%; H, 3.95%; N, 13.73%. Found: C, 50.09%; H, 3.94%; N, 13.70%. FAB-mass (m/z): Obs. (Calcd.) 612.31(612.32 g/mol.); UV-visible (DMSO) λ (nm): 376 (π-π*) and 301 (n-π*). IR data (KBr/cm⁻¹): 1586 (ν>C=N); 604 (νCu-S), 462 and 555 (ν Cu-N).

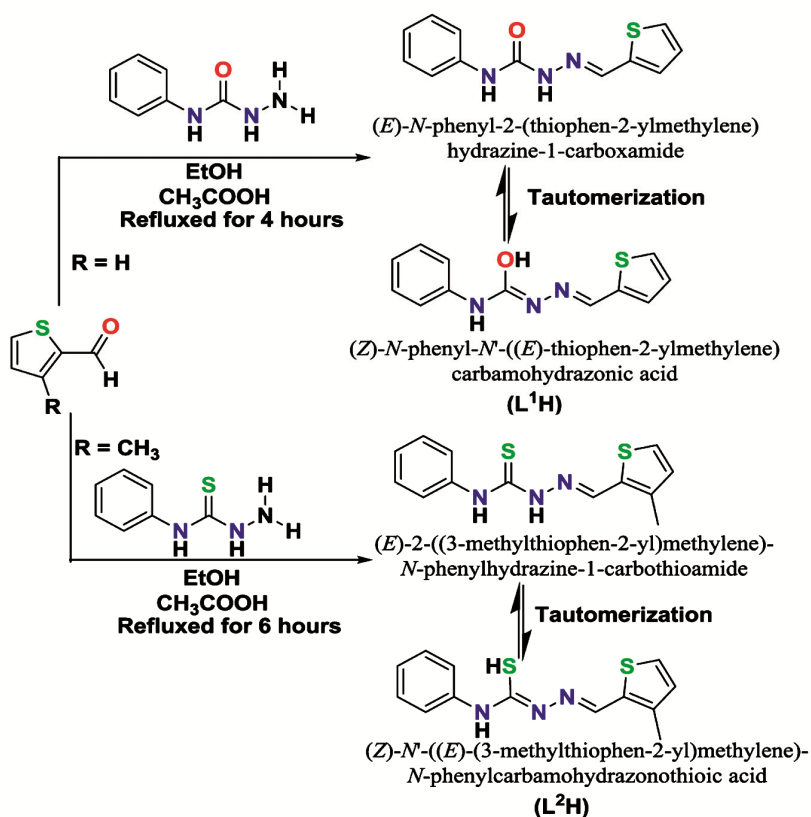
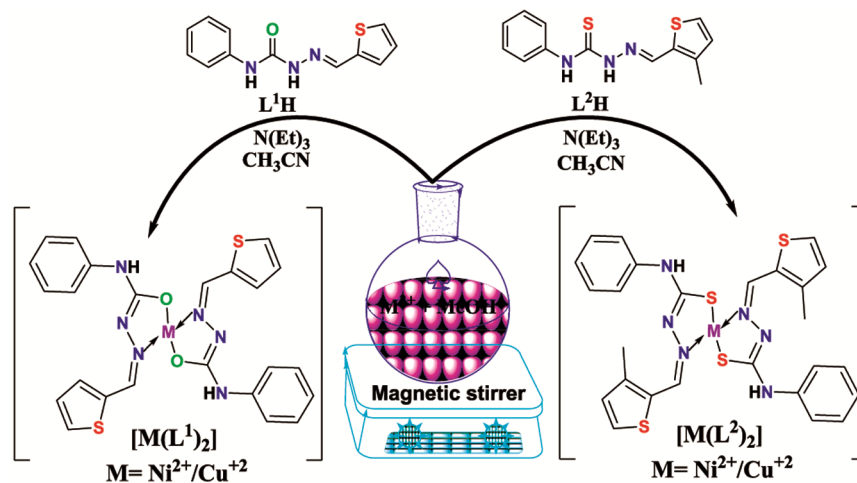
Results and Discussion

Synthesis and characterization

Schiff base ligands **L¹H** and **L²H** were synthesized by condensation reaction of aldehyde and primary amine in 1:1 ratio. All the metal complexes were synthesized in the molar ratio of 1:2 (metal: ligand). The protocol used for their synthesis is given in Schemes 1 and 2. All the synthesized compounds were characterized with different physiochemical and spectroscopy techniques which provide evidence for their formation.

FT-IR and UV-visible spectroscopy

FT-IR of **L¹H** and **L²H** and complexes (3 and 4) were studied. The spectra of **L¹H** and **L²H** shows strong peak for the azomethine imine⁴¹ at 1593 and 1591 cm⁻¹, respectively. The presence of ν(O-H) peak at 3364 cm⁻¹ for **L¹H** indicate that it is present in enol form. The presence of peak at 1283 cm⁻¹ can be assigned to ν(C-O). Also, the presence of ν(S-H) band

Scheme 1 — Synthetic routes for the preparation of Schiff base ligands L^1H and L^2H 

Scheme 2 — Synthetic routes for the Schiff base metal complexes (1)-(4)

at 2326 cm^{-1} for L^2H indicates that the ligand is present in thiol form. On comparison of IR spectra of Schiff base ligand L^2H with the spectra of its metal complexes (3 and 4), the azomethine group is shifted to lower wavelength 1589 cm^{-1} for (3) and 1586 cm^{-1} for (4) and provides evidence for coordination through azomethine nitrogen to the metal ions⁴². Presence of new bands in the region of $543\text{-}555\text{ cm}^{-1}$

and $604\text{-}610\text{ cm}^{-1}$ are the characteristic bands of $\nu(M-N)$ and $\nu(M-S)$ respectively, gives supportive evidence of bonding of L^2H with metal centre. The FT-IR spectra of Schiff base ligands (L^1H and L^2H) and complexes (3 and 4) are presented in supplementary (Figs S5- S8).

The electronic absorption spectra of L^1H and L^2H and complexes (1)-(4) were recorded in DMSO

solvent at RT. UV-visible spectrum of **L¹H** (Fig. S9) shows two bands⁴³, first at 306 nm corresponding to $n \rightarrow \pi^*$ transition in the semicarbazone group, and second one at 340 nm corresponding to $\pi \rightarrow \pi^*$ of the phenyl ring; similarly, for **L²H** (Fig. S10) $n \rightarrow \pi^*$ transition at 325 nm and $\pi \rightarrow \pi^*$ transition at 368 nm. The shift of the bands due to intra ligand transitions is the result of weakening of the C=O/C=S bond and the extension of conjugation upon complexation. A band corresponding to $n \rightarrow \pi^*$ transition was observed at 313, 309, 301 and 283 nm for complex 1-4, respectively. Similarly the band corresponding to $\pi \rightarrow \pi^*$ transition was observed at 348, 350, 376 and 352 nm for complex (1)-(4), respectively. The shift occurs also due to coordination through sulphur/oxygen of thiosemicarbazone/semicarbazone and azomethine nitrogen and is indication of

enolization/thio-enolization followed by deportation of the ligand during complexation. The broadness of these bands can be explained as due to the combination of O \rightarrow Cu/Ni, N \rightarrow Cu/Ni, S \rightarrow Cu/Ni LMCT transitions⁴⁴.

Crystallographic discussion of **L¹H**

White needle shaped crystals of **L¹H** were obtained through slow evaporation from its ethanolic solution at room temperature. The results of X-ray diffraction studies are shown in Table 1. Selected bond distances (Å) and angles (°) are mentioned in Table S1. The **L¹H** crystallized in the trigonal crystal system with the space group R-3: H. Oxygen and nitrogen imine (N1) atoms are in trans-position with respect to the C7-N2 bond⁴³. The molecule displays an E-conformation with respect to C8-N1 bond and is approximately planar due to electron delocalization along the skeleton of the molecule. The ORTEP representation and crystal packing of **L¹H** are presented in Fig. 1. Three-dimensional network is established by comparatively stronger hydrogen bonding in **L¹H** [C (1)-H (1) ...O (1) 0.93 Å, C (12)-H

Table 1 — Crystallographic data and refinement parameters for ligand (L¹H)	
Crystallographic data	Ligand (L¹H)
Formula	C ₁₂ H ₁₁ N ₃ OS
Mw (gmol ⁻¹)	245.30
temp (K)	296(2)
λ (Mo K α) (Å)	1.54178
crystal system	Trigonal
space group	R-3 : H
<i>a</i> (Å)	34.2388(11)
<i>b</i> (Å)	34.2388(11)
<i>c</i> (Å)	5.6225(3)
α (°)	90
β (°)	90
γ (°)	120
<i>V</i> (Å ³)	5708.2(5)
<i>Z</i>	18
<i>D</i> _{calc} (Mg/cm ³)	1.284
μ (mm ⁻¹)	2.169
<i>F</i> (000)	2304
Crystal size (mm ³)	0.300×0.250×0.200
Index ranges	-41<= <i>h</i> <=42, -42<= <i>k</i> <=42, -4<= <i>l</i> <=6
Collected reflections	17117
unique reflections	2453[R(int) = 0.0470]
Absorption correction	Semi-empirical from equivalents
max and min trans	0.7536 and 0.5227
Refinement method	Full-matrix least-squares on <i>F</i> ²
Data / restraints / parameters	2453 / 2 / 162
Goodness-of-fit (GOF) on <i>F</i> ²	1.041 ^a
R1 [<i>I</i> > 2 σ (<i>I</i>)] ^a	0.0389 & 0.0519
wR2 (all data) ^b	0.1024 & 0.1154
CCDC Number	2066722

^aR1 = $\sum ||F_o| - |F_c|| / \sum |F_o|$;
^bwR2 = $\{ \sum [w(F_o^2 - F_c^2)]^2 / \sum [w(F_o^2)]^2 \}^{1/2}$

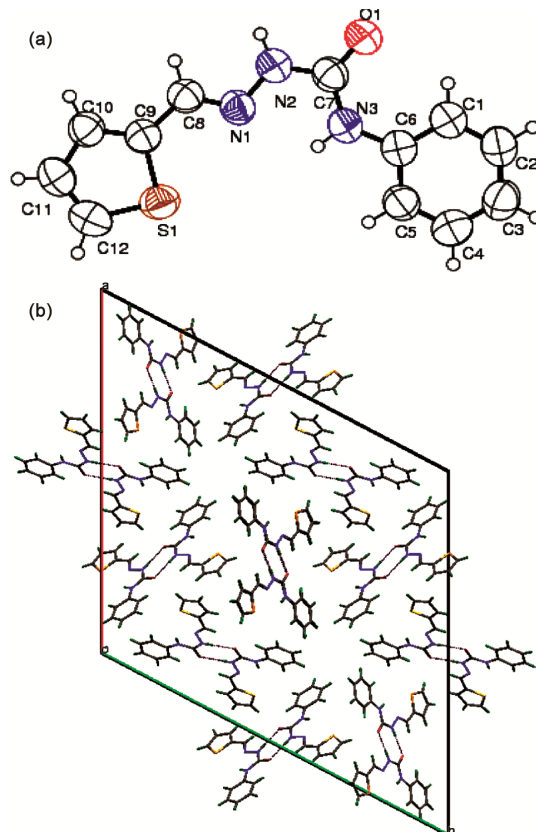


Fig. 1 — (a) ORTEP structure with 50% thermal ellipsoid and with atom numbering scheme and (b) crystal packing view of **L¹H**

(12) ...O (1) 0.93 Å, N(2)-H(2A) ...O (1) 0.877(15) Å and N(3)-H(3A) ...N (1) 0.843(16) Å].⁴⁵(Table 2).

Powder XRD studies

X-ray diffraction studies can provide realistic structural knowledge about the synthesized compounds⁴⁶. After several recrystallization attempts, we were not able to get the single crystals for the synthesized metal complexes. Therefore, we took assistance of powdered XRD studies to test the degree of crystallinity⁴⁷. As shown in Fig. 2, the XRD patterns of the **L¹H** was observed at $2\theta = 22.74^\circ$ which is characteristic peak for a Schiff base imine⁴⁸. XRD pattern of the Ni(II) complex (**1**) shows the sharp crystalline peaks indicating their crystalline phase while that of Cu(II) complex (**2**) does not shows any sharp peak which indicate its amorphous nature. The XRD patterns of the complexes shows almost all peaks of ligand **L¹H** with some new peaks which gives the evidence for the formation of complexes, since the crystalline index of Schiff base ligand **L¹H** at $2\theta = 22.74^\circ$ shifted to $2\theta = 18.2^\circ$ in its complexes due to π - π conjugation between the ligand and metal which confirms the existence of metal ion in the ligand environment. The average crystalline size (*D*) of the complexes was calculated using Scherer's formula⁴⁷,

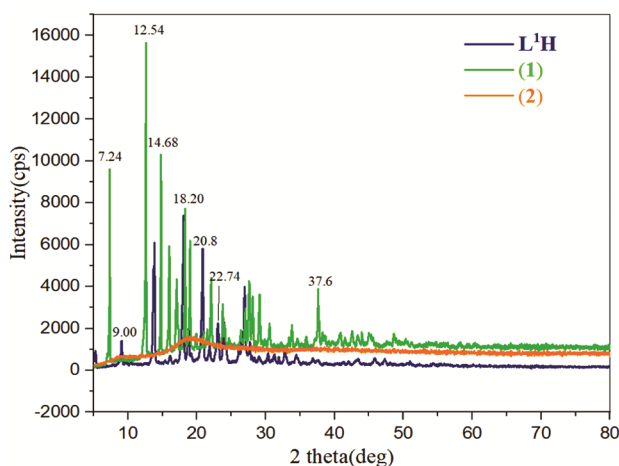


Fig. 2 — Powdered XRD pattern of semicarbazone Schiff base ligand **L¹H** and its Ni(II) (**1**) and Cu(II) complexes (**2**)

and was found to be 46.44 nm for (**1**) and 52.02 nm for (**2**).

Hirshfeld surface analysis

The Hirshfeld surface (HS)⁴⁹ and their relative 2-dimensional (2D) finger print plots for **L¹H** ligand were drawn using the result obtained from a single crystal X-ray by the assistance of Crystal Explorer 3.0. The Hirshfeld surfaces include d_{norm} surface, shape index, and curvedness⁵. The d_{norm} is used to identify the regions of particular importance to intermolecular interaction. The HS for **L¹H** mapped with d_{norm} property is displayed in Fig. S11 and 2-D fingerprint plot analysis with all characteristics features of short interactions are displayed in Fig. S12 and S13. The d_{norm} surface has been mapped over the range of -0.59 to 2.07 au, shape index mapped over -1.0 to 1.0 au, curvedness mapped over -4.0 to 0.4 au while fragment patch mapped over 0.0 to 15 au. These surfaces for **L¹H** were mapped and were drawn transparent to allow visualization of the ligand. Deep red, large spherical depressions visible on the surfaces are evidence of hydrogen-bonding contacts and the weaker and longer contacts other than hydrogen bonding are shown by light coloured small area on the surfaces⁵⁰. Shape index depending on the HS flatness or curvature, blue region shows hydrogen donor groups and a concave red region represents hydrogen acceptor groups. Fingerprint plots depicts that complementary region in plots can be visualized where one molecule behaves as a donor ($d_e > d_i$) while other behaves as an acceptor ($d_e < d_i$). These play an important role to illustrate the comparative contribution in terms of the percentage of various intermolecular interactions in the crystal lattice. It gives a quantitative summary of the nature and type of intermolecular contacts.

The 2D fingerprint plots⁵¹ generated corresponding to the ALL, H...H, C...H, S...H, O...H, and N...H for **L¹H** (Figs S12 and S13). The H...H intermolecular contact is observed to be the most and accounts for 40% of total HS for **L¹H**. The proportion of other significant intermolecular interaction

Table 2 — Hydrogen bonds for Schiff base ligand (**L¹H**) [Å and °]

D-H... A	D (D-H)	d (H... A)	d (D... A)	<(DHA)
C (1)-H (1) ...O (1)	0.93	2.33	2.925(3)	121.3
C (12)-H (12) ...O (1) #1	0.93	2.51	3.310(3)	144.8
N(2)-H(2A) ...O (1) #2	0.877(15)	1.972(16)	2.847(2)	175.4(19)
N(3)-H(3A) ...N (1)	0.843(16)	2.16(2)	2.617(2)	113.9(18)

Symmetry transformations used to generate equivalent atoms: #1 $y-1/3, -x+y+1/3, -z+4/3$ #2 $-x+1/3, -y+2/3, -z+2/3$

C...H/H...C, for L^1H is found to be 24.7%. Further, S...H/H...S (10.3%), O...H/H...O (9.7%), and N...H/H...N (5.7%) are the weak interaction of total HS for L^1H . Fig. 3 display the HS mapped with crystal void and deformation density of the ligand⁵². Crystal void is based on the sum of spherical atomic electron densities at the appropriate nuclear positions (procrystal electron density). The crystal-void calculation (results under 0.002 a.u. iso-value) shows the void volume of the L^1H be of the order of 945.31 Å³ and surface area in the order of 2390.40 Å². The spatial distribution of the electrons involved in the chemical bonding can be studied through deformation density maps. The deformation density (results under 0.008 a.u. iso-value) was mapped over the range 0.008 to -0.008 au. The electron density deformation can be described as the subtraction of the electronic cloud of the molecule, minus the electronic cloud of the promolecule defined as the summation of the free atom spherical electron densities. The deformation is therefore positive between the bonds and negative at the nucleus. Furthermore, energy framework computational analysis⁵³ has been explored for better understanding of the nature of intermolecular interaction energies between the pair of molecules with a 3-D graphical representation of their magnitude. Fig. 4 display the energy framework diagrams for L^1H i.e. dispersion energy (E_{dis}), coulomb energy (E_{coul}), total energy (E_{tot}) and total (annotated) energy ($E_{tot.annot}$) which was calculated by generating a cluster of radii 3.8 Å around the molecule. The interaction energies for L^1H was calculated with CE-[B3LYP/6-31G(d,p)] model displayed in Table S2. It is suggested that the total energy consists of pair wise individual energy profiles such as E_{coul} , E_{dis} , E_{tot} and $E_{tot(annot)}$. The tube size (250) connecting the centroids of the molecule represent the relative strength of the

interaction, and tube colour represents types of energy profiles of the intermolecular interaction energies.

Quantum chemical study

The quantum computation can provide the electrical and chemical properties, which are not possible with conventional characterization instruments due to their intrinsic limitations⁵⁴. Along the similar lines, the computational studies about the coordination compounds have quickly swelled up where it is used with reasonable accuracy to correlate and explain the structural features and functional properties of coordination complexes^{55,56}. All quantum chemical calculations were carried out using the Gaussian 09 program package³⁵. DFT based quantum chemical calculations were performed on Schiff base ligands L^1H and L^2H and their metal complexes (**1-4**) to get the structure property relationship. The FMOs including LUMO and HOMO along with their orbital energies (eV) and energy gaps (eV) for Schiff base ligands L^1H and L^2H are shown in Figs S14 and S15, respectively, while for their metal complexes (**1-4**) are drawn in Fig. 5a-d. Energy gap provide the knowledge about the stability of the compound and chemically stable compounds have larger energy gap⁵⁷. The energy gap values are tabulated in Table 3. During HOMO-LUMO analysis, the relevant occupied and unoccupied Mos (HOMO/LUMO, HOMO-1/LUMO+1 and HOMO-2/LUMO+2) are considered. The LUMO and HOMO energies for L^1H was found to be -9.49 and -11.82 eV; for L^2H -9.61 and -10.91 eV; for (**1**) 0.63 and 0.06 eV; for (**2**) 0.66 and 0.61 eV; for (**3**) 0.25 and -0.24 eV and for (**4**) 0.85 and 0.249 eV, respectively. The energy gap (0.60 eV) for complex (**4**) was found to be highest among all the complexes indicating that it is the most stable complex. The data of FMO are used to calculate the global reactivity

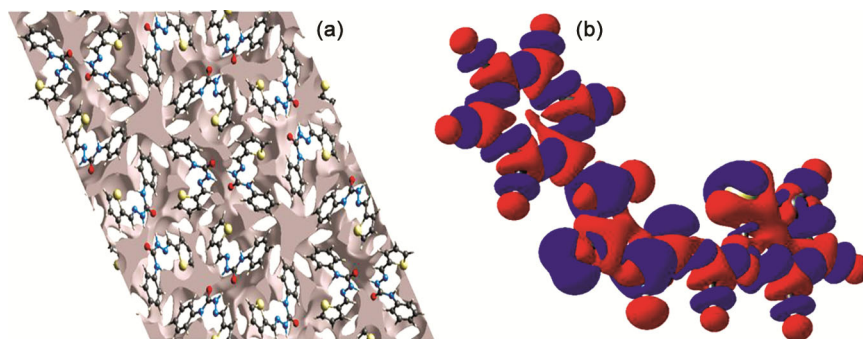


Fig. 3 — HS mapped with (a) Crystal Void (b) deformation energy of L^1H

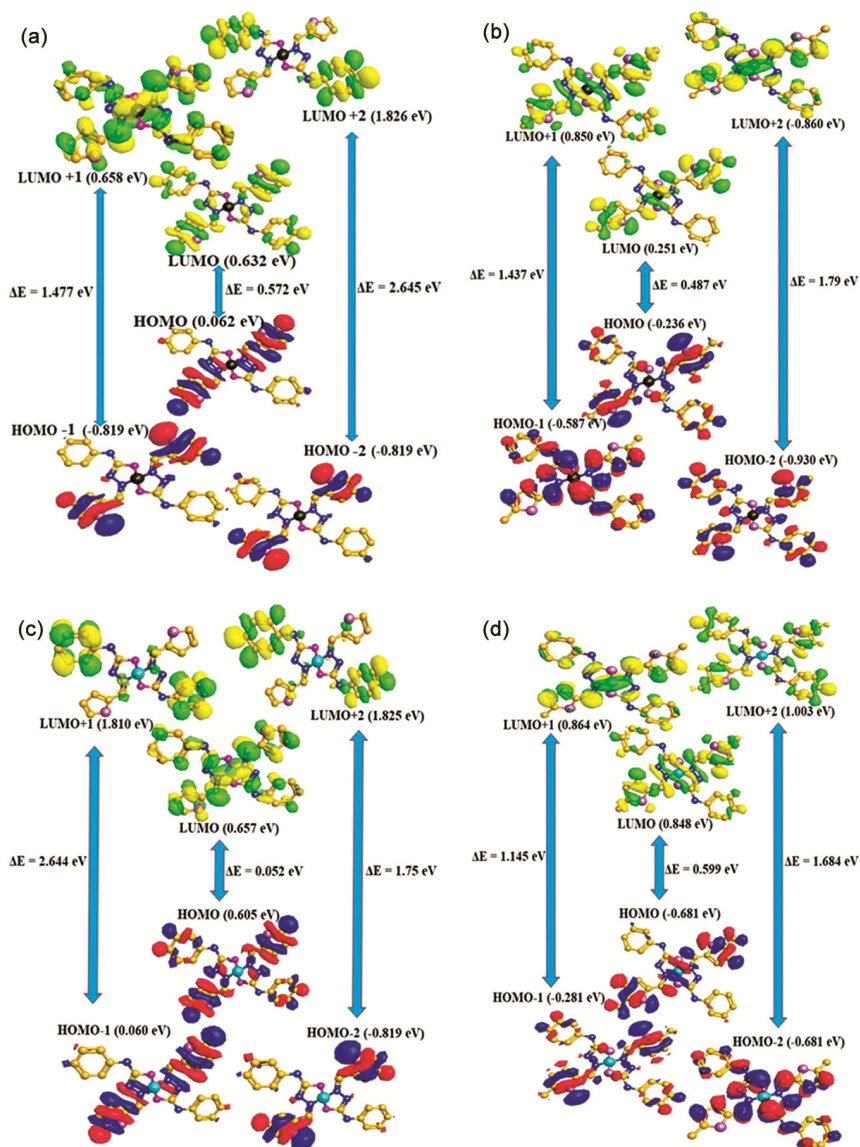


Fig. 5 — Frontier molecular orbitals diagram of nickel(II) complex (a) $[\text{Ni}(\text{L}^1)_2]$ (1), (b) $[\text{Ni}(\text{L}^2)_2]$ (2), (c) $[\text{Cu}(\text{L}^1)_2]$ (3) and (d) $[\text{Cu}(\text{L}^2)_2]$ (4)

Table 3 — HOMO and LUMO energies and energy gap (ΔE)^a of Schiff base ligand L^1H and L^2H and their metal(II) complexes (1)-(4)

Compound	E_{LUMO}	E_{HOMO}	ΔE	$E_{\text{LUMO}+1}$	$E_{\text{HOMO}-1}$	ΔE	$E_{\text{LUMO}+2}$	$E_{\text{HOMO}-2}$	ΔE
L^1H	-9.49	-11.82	2.33	-8.49	-12.11	3.6	-8.47	-12.12	3.65
L^2H	-9.61	-10.91	1.3	-9.04	-11.30	2.41	-8.47	-11.45	2.98
(1)	0.63	0.06	0.57	0.66	-0.82	1.48	1.83	-0.83	2.65
(2)	0.66	0.61	0.05	1.81	0.06	1.75	1.83	-0.82	2.64
(3)	0.25	-0.24	0.48	0.85	-0.59	1.44	0.86	-0.93	1.79
(4)	0.85	0.249	0.60	0.86	-0.281	1.15	1.00	-0.681	1.69

The molecular docking poses of the Schiff base ligands L^1H and L^2H inside SARS-CoV-2 (PDB ID: 7VNB) are displayed in Figs S17 and S18. An overview of Fig. S19 shows that the protein residues which interacts with L^1H are ASN-343, SER-371, LEU-368, VAL-367 and ALA-372; while L^2H

interacts with the protein residues ASP-364, CYS-336, LEU-335, PHE-342 and VAL-367. Protein residue ASN-343 and SER-371 form conventional hydrogen bond with S and N atoms present in L^1H . While ASP-364 and CYS-336 form conventional hydrogen bond with L^2H . Further, Pi-Pi stacked

Table 4 — Global reactivity descriptors^a of the Schiff base ligand **L¹H** and **L²H** and their metal(II) complexes (**1**)-(**4**)

Mathematical description	L¹H	L²H	(1)	(2)	(3)	(4)
IP = -E _{HOMO}	11.82	10.91	-0.06	-0.61	0.24	-0.25
EA = -E _{LUMO}	9.49	9.61	-0.63	-0.66	-0.25	-0.85
$\chi = (IP + EA)/2$	10.66	10.26	-0.35	-0.64	-0.005	-0.55
$\eta = (IP - EA)/2$	1.17	0.65	0.29	0.635	0.25	0.3
$\mu = -(IP + EA)/2$	-10.66	-10.26	0.35	0.64	0.005	0.55
$\sigma = 1/2\eta$	0.43	0.77	1.72	0.79	0.02	1.67
$\omega = \mu^2 / 2\eta$	48.86	81.06	0.21	0.32	0.0	0.51

^a Ionization potential (IP), electro negativity (χ), electron affinity (EA), chemical potential (μ), global softness (σ), global hardness (η), units are in eV

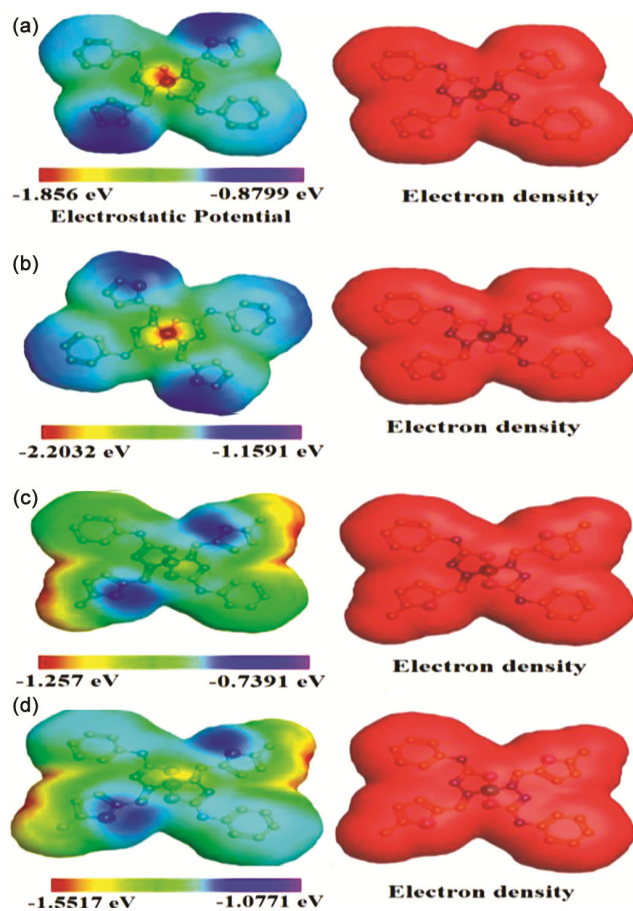


Fig. 6 — Molecular electrostatic potential (MEP) maps and electron density surface representation of metal complexes (**1**)-(**4**)

interaction is also seen between protein residue PHE-342 and **L²H**. Figs S20-S23 display the docking possesses of the metal complexes (**1**)-(**4**) inside SARS-CoV-2 (PDB ID: 7VNB). Fig. 7 represents the 2-D diagrams of different interactions occurring between the metal complexes (**1**)-(**4**) with SARS-CoV-2 (PDB ID: 7VNB). From this figure, it is clear that protein residues ILE-69 shows convection hydrogen bond⁵⁹ with complex (**1**), GLU-46 and VAL-445 show convection hydrogen bond with complex (**2**), GLY-105, ASN-98, SER-28 and ASP-31 show convection

hydrogen bond with complex (**3**) while ASP-428 shows convection hydrogen bond with complex (**4**). Pi-Pi T-shaped interaction occur between protein residue TYR-58 and phenyl ring of complex (**1**), while protein residue TYR-396 also shows pi-pi T-shaped interaction with phenyl ring of complex (**4**). The binding affinities of free Schiff base ligands are found to be less than their corresponding metal complexes. The binding affinities for Schiff base ligands **L¹H** and **L²H** and their metal complexes (**1**)-(**4**) are -7.5, -7.2, -8.8, -8.5, -9.1 and -9.9 kcal/mol, respectively.

370, ALA-408, GLN-407, ARG-358 and VAL-108; while **L²H** interacts with the protein residues GLN-407, GLN-407, TYR 232, TYR-232, GLN-407, VAL-108 and ALA-408. Figs S27-S30 display the docking possess of the metal complexes (**1**)-(**4**) inside HIV-1 virus (PDB ID: 1REV). Fig. 8 represents the 2-D diagrams of different interactions occurring between the metal complexes (**1**)-(**4**) with HIV-1 virus (PDB ID: 1REV). From Figure 22 it is clear that protein residues TYR-181 and MET-14 show convection hydrogen bond with complex (**1**), GLY-384 shows convection hydrogen bond with complex (**2**), ASN-137 shows convection hydrogen bond with complex (**3**) while GLY-384, TYR-181, PRO-95 and LYS-154 show convection hydrogen bond with complex (**4**). Pi-Pi T-shaped interaction occur between protein residue ILE-94 and phenyl ring of complex (**1**), while protein residue pro-157 also shows pi-pi T-shaped interaction with phenyl ring of complex (**4**). The binding affinities of free Schiff base ligands are found to be less than their corresponding metal complexes⁶⁰. The binding affinities for Schiff base ligands **L¹H** and **L²H** and their metal complexes (**1**)-(**4**) are -6.2, -6.1, -7.8, -7.3, -7.7 and -7.9 kcal/mol, respectively. It was observed that the binding affinities of the Schiff bases and metal complexes towards SARS-CoV-2 were comparatively higher than the HIV virus. This study may offer the new

Table 5 — The molecular docking results for Schiff base ligand **L¹H** and **L²H** and their metal(II) complexes (**1**)-(4) with M^{Pro} (PDB ID: 7VNB) including the binding affinity, inhibition constant and different amino acid residues of M^{Pro} that interact with the compounds

Molecule	Binding affinity (kcal/mol)	Interacting residues		
		H-bond	Electrostatic	Hydrophobic
L¹H	-7.5	ASN-343 (2.72 Å) SER-371 (2.07 Å)	LEU-368 (3.12 Å)	VAL-367 (4.79 Å) ALA-372 (4.02 Å)
L²H	-7.2	ASP-364 (3.64 Å) CYS-336 (2.03 Å) CYS-336 (2.52 Å)	LEU-335 (3.7 Å) PHE-342 (5.45 Å)	VAL-367 (4.74 Å)
(1)	-8.8	ILE-69 (2.68 Å)	LYS-64 (4.24 Å)	ARG-56 (3.65 Å) TYR-58 (5.23 Å) ILE-59 (5.17 Å) LYS-64 (5.44 Å)
(2)	-8.5	GLU-46 (2.12 Å) VAL-445 (2.46 Å) LYS-43 (2.93 Å)	LYS-43 (4.98 Å)	LYS-444 (4.61 Å) LYS-43 (4.11 Å) LYS-444 (5.14 Å)
(3)	-9.1	ASN-98 (2.28 Å) ASP-31 (2.67 Å) SER-28 (2.45 Å) ASP-31 (2.22 Å) GLY-105 (2.60 Å)	TYR-32 (5.69 Å)	TYR-32 (5.03 Å) ILE-468 (4.41 Å) ILE-468 (4.92 Å)
(4)	-9.9	ASP-428 (2.25 Å) PHE-515 (3.22 Å) ASP-428 (3.51 Å)	ARG-355 (4.03 Å) PHE-464 (5.68 Å)	TYR-396 (4.85 Å) PHE-464 (5.31 Å) LEU-517 (5.42 Å) PRO-426 (5.38 Å) PRO-463 (3.72 Å)

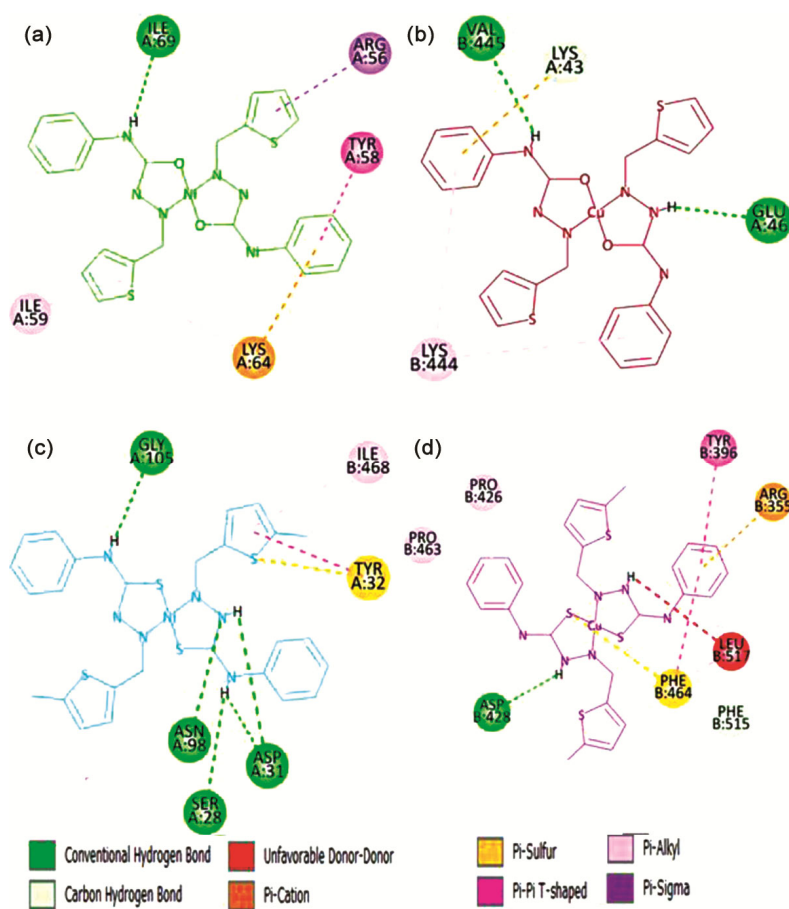
Table 6 — The molecular docking results for Schiff base ligand **L¹H** and **L²H** and their metal(II) complexes (**1**)-(4) with HIV virus (PDB ID: 1REV) including the binding affinity, inhibition constant and different amino acid residues of HIV virus that interact with the compounds

Molecule	Binding affinity (kcal/mol)	Interacting residues		
		H-bond	Electrostatic	Hydrophobic
L¹H	-6.2	TYR-232 (2.67 Å)	GLU-370 (3.61 Å)	ALA-408 (3.92 Å) GLN-407 (4.36 Å) ARG-358 (5.23 Å) VAL-108 (5.40 Å)
L²H	-6.1	GLN-407 (2.55 Å) GLN-407 (2.21 Å)	TYR-232 (4.07 Å)	TYR-232 (3.90 Å) GLN-407 (4.78 Å) VAL-108 (5.28 Å) ALA-408 (4.12 Å)
(1)	-7.8	MET-184 (2.77 Å) TYR-181 (2.50 Å) GLY-384 (3.44 Å)	PRO-95 (4.74 Å)	MET-184 (3.97 Å) ILE-94 (4.74 Å) LYS-385 (5.08 Å) LYS-154 (4.43 Å) PRO-157 (5.47 Å) ALA-158 (4.65 Å) ILE-94 (5.03 Å)

(contd.)

Table 6 — The molecular docking results for Schiff base ligand L^1H and L^2H and their metal (II) complexes (1)-(4) with HIV virus(PDB ID: 1REV) including the binding affinity, inhibition constant and different amino acid residues of HIV virus that interact with the compounds (*contd.*)

Molecule	Binding affinity (kcal/mol)	Interacting residues		
		H-bond	Electrostatic	Hydrophobic
(2)	-7.3	GLY-384 (2.31 Å)	LYS-154 (4.74 Å) LYS-385 (4.43 Å)	TYR-319 (3.21 Å) LYS-154 (4.00 Å) MET-184 (3.62 Å) PHE-87 (6.00 Å) ILE-94 (4.75 Å) PRO-157 (5.31 Å) LYS-385 (4.69 Å)
(3)	-7.7	ASN-137 (2.85 Å) GLN-23 (2.84 Å)	ILE-135 (4.63 Å)	TRP-24 (4.71 Å) VAL-381 (4.72 Å) PRO-25 (4.28 Å) LYS-22 (5.26 Å)
(4)	-7.9	GLY-384 (2.8 Å) LYS-154 (2.10 Å)	PRO-95 (2.98 Å) TYR-181 (2.21 Å)	PRO-157 (4.90 Å) LYS-385 (4.63 Å) ILE-94 (5.18 Å) PRO-157 (5.05 Å) ALA-158 (4.29 Å) ILE-94 (4.74 Å)

Fig. 7 — 2-D representation of docked metal complexes (1)- (4) inside the SARS-CoV M^{Pro}(7VNB) with its focused view for interacting residues around the docked complex

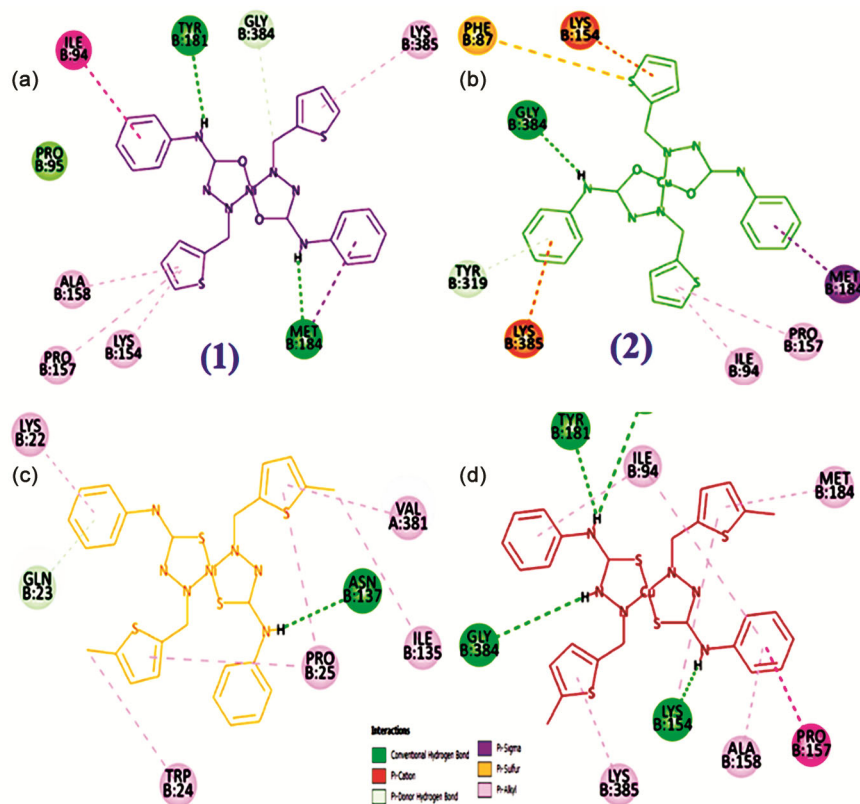


Fig. 8 — 2-D representation of docked metal complexes (1)- (4) inside the HIV virus (1REV) with its focused view for interacting residues around the docked complex

antivirus drug candidates against SARS-CoV-2 and HIV virus⁶¹.

Conclusion

We have designed a series of nickel(II) and copper(II) (**1-4**) complexes using Schiff base ligands (**L¹H**- **L²H**). Different physicochemical and spectroscopy techniques were used to characterize the synthesized complexes which provide evidence for their formation. Single-crystal X-ray diffraction reveals that **L¹H** is crystallized in the trigonal crystal system with the space group R-3: H. The oxygen and nitrogen imine (N1) atoms are in trans-position with respect to the C7-N2 bond¹. The molecule displays an E-conformation with respect to C8-N1 bond and is approximately planar due to electron delocalization along the skeleton of the molecule. The Hirshfeld surface (HS) for **L¹H** is analyzed to evaluate the intermolecular interaction in the crystal system. Powdered XRD studies were done for **L¹H** and its corresponding metal complexes (**1**) and (**2**). XRD patterns of the Ni(II) complex (**1**) shows the sharp crystalline peaks indicating their crystalline phase while that of Cu(II) complex (**2**) does not show any

sharp peak which indicate its amorphous nature. We have successfully docked all the synthesized compounds with the main protease (M^{Pro}) of protein (PDB ID: 7VNB) of SARS-CoV-2 and HIV-1 virus (PDB ID: 1REV). Molecular docking result reveals that all the synthesized compounds shows higher binding energy against the main protease (M^{Pro}) of protein (PDB ID: 7VNB) of SARS-CoV-2 than HIV-1 virus (PDB ID: 1REV). Considering all the results, it is clear that all synthesized compounds exhibited pharmacokinetics response.

Supplementary Information

Supplementary information is available in the website <http://nopr.niscpr.res.in/handle/123456789/58776>. Deposition Number: CCDC-2066722 for Schiff base ligand (**L¹H**) contains the supplementary crystallographic data for this paper. This data can be obtained free of charge at www.ccdc.cam.ac.uk/conts/retrieval.html or www.ccdc.cam.ac.uk/structures or from the Cambridge Crystallographic Data Center, 12 Union Road, Cambridge CB2 1EZ, UK; fax: +44 1223/ 336 033. Email: deposit@ccdc.ac.uk.

Acknowledgement

We thank SAIF, IIT Madras for Single crystal X-ray analysis of Schiff base ligand (L^1H). Also thanks to SAIF, IIT Madras for spectral analysis (NMR and IR analysis). The authors are thankful to the Head, Chemistry Department, National Institute of Technology Patna for providing computational resources and spectral analysis. One of the authors (Aprajita) thanks to CSIR, New Delhi, India for awarding JRF fellowship (File no. 09/1278(0003)/2020-EMR-I).

References

- Casas J S, Garcia-Tasende M S & Sordo J, *Coord Chem Rev*, 209 (2000) 197.
- dos Santos S F F, Oliveira A A, Santos G R, Mahmoudi G, Afkhami F A, Santiago P S, Viana R B, da Silva A B F & Santos R H A, *J Mol Struct*, 1197 (2019) 393.
- Beraldo H & Gambino D, *Mini Rev Med Chem*, 4 (2004) 31.
- Lobana T S, Sharma R, Bawa G & Khanna S, *Coord Chem Rev*, 253 (2009) 977.
- Savir S, Wei Z J, Liew J W K, Vythilingam I, Lim Y A L, Saad H M, Sim K S & Tan K W, *J Mol Struct*, 1211 (2020) Article 128090.
- Pelosi G, Bisceglie F, Bignami F, Ronzi P, Schiavone P, Re M C, Casoli C & Pilotti E, *J Med Chem*, 53 (2010) 8765.
- Rui W, Tian X, Zeng P, Liu W, Ying P, Chen H, Lu J, Yang N & Chen H, *Polyhedron*, 117 (2016) 803.
- Khanye S D, Smith G S, Lategan C, Smith P J, Gut J, Rosenthal P J & Chibale K, *J Inorg Biochem*, 104 (2010) 1079.
- F Bisceglie, N Orsoni, M Pioli, B Bonati, P Tarasconi, C Rivetti, D Amidani, S Montalbano, A Buschini & G Pelosi, *Metallomics*, 11 (2019) 1729.
- Fallah-Mehrjardi M, Kargar H, Behjatmanesh-Ardakani R, Ashfaq M, Munawar K S & Tahir M N, *J Mol Struct*, 1251 (2022) Article 132037.
- Yu H, Zhang W, Yu Q, Huang F P, Bian H D & Liang H, *Molecules*, 22 (2017) 1772.
- Tyagi P, Chandra S & Saraswat B S, *Spectrochim Acta Part A*, 134 (2015) 200.
- Kargar H, Ardakani A A, Tahir M N, Ashfaq M & Munawar K S, *J Mol Struct*, 1229 (2021) Article 129842.
- Kumar D, Chandhel V, Raj S & Rathi B, *Chem Biol Lett*, 7 (2020) 166.
- Bhatia S, Giri S, Lal A F & Singh S, *Trop Med Health*, 1 (2020) 21.
- Kozak J J, Gray H B & Garza-Lopez R A, *J Inorg Biochem*, 211 (2020) Article 111179.
- Sang P, Tian S H, Meng Z H & Yang L Q, *RSC Adv*, 10 (2020) 15775.
- Zhang L, Lin D, Sun X, Curth U, Drosten C, Sauerhering L, Becker S, Rox K & Hilgenfeld R, *Science*, 368 (2020) 409.
- Hatada R, Okuwaki K, Mochizuki Y, Handa Y, Fukuzawa K, Komeiji Y, Okiyama Y & Tanaka S, *J Chem Info Model*, 60 (2020) 3593.
- Zang S, Krumberger M, Morris M A, Parrocha C M T, Kreutzer A G & Nowick J S, *Eur J Med Chem*, 218 (2021) Article 113390.
- Zhang L, Lin D, Kusov Y, Nian Y, Ma Q, Wang J, Brunn A V, Leyssen P, Lanko K, Neyts J, Wilde A D, Snijder E J, Liu H & Hilgenfeld R, *J Med Chem*, 63 (2020) 4562.
- Jin Z, Du X, Xu Y, Deng Y, Liu M, Zhao Y, Zhang B, Li X, Zhang L, Peng C, Duan Y, Yu J, Wang L, Yang K, Liu F, Jiang R, Yang X, You T, Liu X, Yang X, Bai F, Liu H, Liu X, Guddat L W, Xu W, Xiao G, Qin C, Shi Z, Jiang H & Rao Z, *Nature*, 582 (2020) 289.
- Sheldrick G M, *Acta Crystallogr C*, C71 (2015) 3.
- Brandenburg K, *Diamond version 3 2k*, (Crystal Impact GbR, Bonn, Germany) 2014
- Chavan S S & Sawant V A, *J Mol Struct*, 965 (2010) 1.
- Ide S, Anc N, Oztas S G & Tuzun M, *J Mol Struct*, 562 (2001) 1.
- Turner M J, Mckinnon J J, Wolff S K, Grimwood D J, Spackman P R, Jayatilaka D & Spackman M A, *Crystal Explorer 17*, (The University of Western Australia, Australia) 2017.
- Hirshfeld F L, *Theoretica chimica acta*, 44 (1977) 129.
- Kumara K, Kumar A D, Kumar K A & Lokanath N K, *Chem Data Collect*, 13 (2018) 40.
- Mackenzie C F, Spackman P R, Jayatilaka D & Spackman M A, *IUCrJ*, 4 (2017) 575.
- Kumar S M, Lakshminarayana B N, Nagaraju S, Ananda S, Manjunath B C, Lokanath N K & Byrappa K, *J Mol Struct*, 1173 (2018) 300.
- Frisch M J, Trucks G W, Schlegel H B, Scuseria G E, Robb M A, Cheeseman J R, Scalmani G, Barone V, Mennucci B & Petersson G A, *Gaussian 16 Rev A03*, (Wallingford, CT) 2016.
- Lambert H, Mohan N & Lee T C, *Phys Chem Chem Phys*, 21 (2019) 14521.
- Chai J D & Gordon M H, *Phys Chem Chem Phys*, 10 (2008) 6615.
- Koopmans T, *Physica*, 1 (1934) 104.
- Yang Z, Wang Y, Jin Y, Zhu Y, Wu Y, Li C, Kong Y, Song W, Tian X, Zhan W, Huang A, Zhou S, Xia S, Tian X, Peng C, Chen C, Shi Y, Hu G, Du S, Wang Y, Xie Y, Jiang S, Lu L, Sun L, Song Y & Ying T, *Signal Transduct Target Ther*; 6 (2021) 378.
- Ren J, Esnouf R, Hopkins A, Ross C, Jones Y, Stammers D & Stuart D, *Structure*, 3 (1995) 915.
- Park H, Lee J & Lee S, *Proteins*, 65 (2006) 549.
- Seeliger D & de Groot B L, *J Comput Aided Mol Des*, 24 (2010) 417.
- Biovia D S, *Discovery Studio Visualizer*, v17 2 0 16349, (Dassault Systems, San Diego) 2016.
- Savir S, Liew J W K, Vythilingam I, Lim Y A L, Tan C H, Sim K S, Lee V S, Maah M J & Tan K W, *J Mol Struct*, 1242 (2021) Article 130815.
- Latheef L, Kurup M R P & Suresh E, *Chem Data Coll*, 35 (2021) 100758.
- Nehar O K, Mahboub R, Louhibi S, Roisnel T & Aissaoui M, *J Mol Struct*, 1204 (2010) Article 127566.
- Jacob J M, Kurup M R P, Nisha K, Serdaroglu G & Kaya S, *Polyhedron*, 189 (2020) Article 114736.
- Basri R, Khalid M, Shafiq Z, Tahir M S, Khan M U, Tahir M N, Naseer M M & Braga A A C, *ACS Omega*, 5 (2020) 30176.
- Jawoor S S, Kumbar M & Patil S A, *Appl Organometal Chem*, 32 (2018) e4322.

- 47 Nair M S, Arish D & Joseyphus R S, *J Saudi Chem Soc*, 16 (2012) 83.
- 48 Biswasa M, Sanudo E C, Cirera J & Ray D, *New J Chem*, 44 (2020) 4812.
- 49 Rapheal P F, Manoj E, Kurup M R P & Fun H, *J Mol Struct*, 1237 (2021) Article 130362.
- 50 Vineetha M C, Joy F, Murali K P, Vinod T P, Venkataraman S K, Agarwal A K, Nair Y & Kurup M R P, *Appl Organomet Chem*, 35 (2021)e6334.
- 51 Hashim K K M, Manoj E & Kurup M R P, *J Mol Struct*, 1246 (2021) Article 131125.
- 52 Kumar S & Chodhary M, *J Biomol Struct Dyn*, (2021) 1.
- 53 Kumar S & Choudhary M, *New J Chem*, 46 (2022) 4911.
- 54 Parr R G, Szentpaly L & Liu S, *J Am Chem Soc*, 121 (1999) 1922.
- 55 Patel R N, Patel S K, Kumhar D, Patel N, Patel A K, Jadeja R N, Patel N, Butcher B J, Carijo M & Herrero S, *Polyhedron*, 188 (2020) Article 114687.
- 56 Murray J J & Politzer P, *WIREs Comput Mol Sci*, 1 (2011) 153.
- 57 Murugavel S, Velan V V, Kannan D & Bakthadoss M, *J Mol Struct*, 1108 (2016) 150.
- 58 Boopathi S, Poma A B & Kolandaivel P, *J Biomol Struct Dyn*, (2020) 1.
- 59 Ali A, Sepay N, Afzal M, Sepay N, Alarifi A, Shahid M & Ahmad M, *Bioorg Chem*, 110 (2021) Article 104772.
- 60 Shanty A A, Raghu K G & Mohanan P V, *J Mol Struct*, 1197 (2019) 154.
- 61 McMahon J H, Zerbato J M, Lau J S Y, Lange J L, Roche M, Tumpach C, Dantanarayana A, Rhodes A, Chang J, Rasmussen T A, Mackenzie C A, Alt K, Hagenauer M, Roney J, O'Bryan J, Carey A, McIntyre R, Beech P, O'Keefe G J, Wichmann C W, Scott F E, Guo N, Lee S T, Liu Z, Caskey M, Nussenzweig M C, Donnelly P S, Egan G, Hagemeyer C E, Scott A M & Lewin S R, *EBioMedicine*, 65 (2021) Article 103252.